Title

Eulerian thermo-mechanical simulations of heterogeneous solid propellants using an approximate projection method

Authors

Kumar, Tadbhagya
Rycroft, Chris H
Jackson, Thomas L

Publication Date

2020-09-01

DOI

10.1016/j.combustflame.2020.05.023

Eulerian Thermo-mechanical Simulations of Heterogeneous Solid Propellants using an Approximate Projection Method

Tadbhagya Kumar[a], Chris H. Rycroft[b,c], Thomas L. Jackson[a,*]

[a] *Department of Mechanical and Aerospace Engineering, University of Florida, Gainesville, FL*
[b] *John A. Paulson School of Engineering and Applied Sciences, Harvard University, Cambridge, MA*
[c] *Computational Research Division, Lawrence Berkeley Laboratory, Berkeley, CA*

Abstract

We present a mathematical model that describes thermo-mechanical deformations and thermal gradients on the unsteady burning of a heterogeneous solid propellant. A scaling study shows that the deformations in solid at combustion timescales can be treated as quasi-static. The resulting thermo-mechanical formulation is formulated on a Cartesian grid and makes use of a weak form of Chorin-type projection method to deal with large difference in shear modulus of constituent materials. A one-dimensional verification study is carried out by comparing numerical simulations with those of an analytical model. In addition, convergence studies for a two-dimensional propellant sandwich configuration are presented for the stress, velocity, and reference map components. Finally, simulations are carried out for a two-dimensional random propellant pack and the time-averaged burn rate and strains are reported.

Keywords: Heterogeneous propellant, thermo-mechanical, approximate projection method, simulations

1. Introduction

Heterogeneous solid propellants find prevalent use in space missions, rockets, missiles, etc., which makes understanding the underlying physics that influences their combustion critical to the design process. To supplement experiments that are often expensive to conduct, it is desirable to have computational frameworks able to carry out physics-based simulations. Hence, propellant combustion modeling has been the focus of researchers and companies to design better rockets for the last few decades.

A typical solid propellant consists of an energetic material such as ammonium perchlorate (AP) embedded in a polymeric binder matrix [1]. The constituent materials have different thermal and mechanical properties, thus any framework of interest should be robust enough to handle the discontinuities arising from heterogeneity. Numerical simulation of propellant combustion is severely challenging owing to the multi-physics nature of the problem: complex chemical reactions giving rise to gas products, a dynamic burning surface

*Corresponding author
Email address: tlj@ufl.edu (Thomas L. Jackson)

separating the solid and gas phase, heat transfer between the two phases driving combustion, and thermo-mechanical deformations within the solid caused by high temperatures and chamber pressure. The propellant combustion problem has garnered attention over the past two decades with significant progress being made on three-dimensional modeling of random packs. Early modeling efforts included burning sandwich configuration (strips of AP and binder arranged alternatively) or periodic arrays of AP particles in binder. However, these packs are not representative of actual propellant morphology. Knott *et al.* [2] presented a framework for generating truly random three-dimensional heterogeneous packs using the Lubachevsky and Stillinger's algorithm [3]. To model combustion physics, one of the earliest efforts consisted of modeling the gas phase using Oseen's approximation for the momentum equation, the energy and species equations, a pyrolysis law to describe surface evolution, and unsteady heat conduction in the solid phase. Hegab *et al.* [4] presented one such analysis where both the solid and gas phases were completely coupled, and solved the unsteady heat conduction in both phases with Oseen's approximation in the gas phase. This reduces the momentum equation to quasi-one dimension to model the vertical gas velocity. Successive modeling extended the Oseen approximation to use the low Mach number Navier–Stokes equations [5] for the gas phase. Wang *et al.* [6] extended the propellant combustion framework to include aluminized propellants. Jackson[7] provides a comprehensive review of research conducted in this domain. However, all of these modeling efforts account only for unsteady heat conduction in the solid phase, neglecting thermo-mechanical effects.

The study of mechanical response has largely focused on the macroscopic matrix behavior and constitutive models for porosity, and capturing the viscoelastic response of the damaged binder matrix [8, 9, 10]. The porosity is caused by dewetting, a phenomenon where AP particles dissociate from binder leading to the formation of voids. This serves to alter the macroscopic binder response by reducing the bulk modulus of the matrix. These studies capture the mechanical response to straining, but do not account for near-surface thermal deformations. To this end, Kuznetsov and Stewart [11] presented a one-dimensional analytical and numerical study for homogeneous propellants using a small-strain approximation. They observed a decrease in surface temperature because thermal expansion absorbs heat near the surface. Srinivasan *et al.* [12] carried out two-dimensional studies of heterogeneous packs using a compressible hyperelastic model and found decreased regression rates for deformable propellants. They observed large thermo-mechanical strains at the AP-binder interface, within the thermal boundary layer. This could point to possible hot-spots for damage at the microscopic level, which could possibly propagate within the propellant. These findings motivate this work as we seek to develop a predictive framework capable of identifying highly strained areas in the propellant pack near the burning surface. Our goal is to carry out numerical simulations that account for the coupling between both phases and solve for temperature, stresses, and strains in the solid phase, for which an Eulerian framework is desired.

Since the regressing surface has a complex topology, a Lagrangian approach would require mesh generation

at each time step. A fully Eulerian approach has its advantages in the fact that both phases are on the same grid, which saves computational effort of grid generation. In an Eulerian setting, surface tracking can be achieved either through level sets [13, 6] or by coordinate transformations that map a corrugated surface to a flat one [4, 5, 14]. While the choice of an Eulerian framework simplifies the computational aspect of the problem, it becomes challenging to provide a mathematical description of the mechanical behavior. To describe the stress state, it is routine to use a strain energy potential that is assumed to be a function of the deformation gradient and temperature [15, 12]. To specify the deformation gradient, explicit information about the current location of material points is needed. In an Eulerian system, this is much more difficult to do since material points are not explicitly tracked. One of the popular ways is to use a hypoelastic constitutive law, which postulates a rate equation of the stress tensor in terms of deformation rate [16] and has been used for problems involving finite strains and elasto-plastic deformations [17, 18, 19, 20]. Other approaches include defining the deformation gradient [21, 22, 23], or a reference map [24], as the primitive variable on the grid and specifying a conservation law. The updated deformation gradient can then be coupled with a hyperelastic law to simulate finite strain mechanics. It can be shown that in the limit of small strains, hyperelasticity and hypoelasticity converge.

In this work, a two-dimensional burning heterogeneous solid propellant system consisting of AP particles in a hydroxyl-terminated-poly-butadiene (HTPB) binder is considered with a focus on thermo-mechanical deformations in the solid phase. Both constituent materials are treated as hypoelastic solids. We do not consider coupling to the gas phase combustion processes. Instead, we assume a constant heat flux from the gas phase driving the solid pyrolysis. In addition plastic deformations in the solid phase are neglected. The effect of thermal deformations in the solid phase is taken into account through an additive decomposition of the deformation gradient tensor $\mathbf{D}$ into elastic and thermal parts, i.e. $\mathbf{D} = \mathbf{D}_e + \mathbf{D}_{th}$. The temperature is obtained from the energy equation with the stress work term to capture the dissipative effect of deformations. A scaling analysis is used to motivate the quasi-static nature of the problem and the resulting choice of approximate projection method is then presented along with numerical discretization of the governing equations on a Cartesian grid. For code verification studies, we use a one-dimensional test case for the propellant constituent materials, as well as a two-dimensional sandwich configuration. Results are then presented for a two-dimensional random propellant pack and subsequent findings are discussed.

2. Governing Equations

The thermo-mechanical response in the form of a general theory has been the subject of extensive research, and there are several frameworks that describe this behavior of solids, hypoelasticity being one of them. It is assumed that the stress rate is linearly dependent on the deformation rate tensor and the constitutive

relation is assumed to be

$$\dot{\boldsymbol{\sigma}}_{\boldsymbol{J}} = \mathbf{C} : \mathbf{D}_e, \tag{1}$$

where $\dot{\boldsymbol{\sigma}}$ is a measure of stress rate, $\mathbf{D}_e$ is the elastic deformation rate tensor, and $\mathbf{C}$ is the fourth order material stiffness. Since the stress rate is not objective, there exist different definitions of objective stress rates, with the Jaumann rate [15] being the most popular one. It is defined as

$$\dot{\boldsymbol{\sigma}}_{\boldsymbol{J}} = \frac{\partial \boldsymbol{\sigma}}{\partial t} + \mathbf{v} \cdot \nabla \boldsymbol{\sigma} + \boldsymbol{\sigma} \cdot \boldsymbol{\omega} - \boldsymbol{\omega} \cdot \boldsymbol{\sigma}, \tag{2}$$

where $\mathbf{v}$, $\boldsymbol{\sigma}$, and $\boldsymbol{\omega}$ are the velocity, Cauchy stress tensor, and spin tensor, respectively. For a linear isotropic material with shear modulus μ and bulk modulus K, $C_{ijkl} = \lambda \delta_{ij}\delta_{kl} + \mu(\delta_{il}\delta_{jk} + \delta_{ik}\delta_{jl})$, where $\lambda = K - \frac{2\mu}{3}$. The total rate-of-deformation tensor is defined as

$$\mathbf{D} = \frac{1}{2}\left(\nabla \mathbf{v} + \nabla \mathbf{v}^{\mathsf{T}}\right). \tag{3}$$

Using the additive decomposition, $\mathbf{D}$ is assumed to be a linear combination of elastic, plastic, and thermal parts [25], so that

$$\mathbf{D} = \mathbf{D}_e + \mathbf{D}_p + \mathbf{D}_{th}. \tag{4}$$

In this work, we neglect plastic deformation and thus $\mathbf{D}_p = \mathbf{0}$. The thermal deformation $\mathbf{D}_{th}$ is stated as the rate form of linear expansion used in small strain theory [26],

$$\mathbf{D}_{th} = \alpha \dot{T} \mathbf{I}, \tag{5}$$

where $\alpha, K, \dot{T}, \boldsymbol{I}$ are the thermal expansion coefficient, bulk modulus, the time derivative of temperature, and second order identity tensor, respectively. The conservation of momentum can be written as

$$\rho \frac{d\mathbf{v}}{dt} = \nabla \cdot \boldsymbol{\sigma} + \mathbf{b}_f, \tag{6}$$

where ρ is the density of the material, $\mathbf{v}$ the velocity vector, and $\mathbf{b}_f$ the body force. The temperature distribution in the solid is obtained from the energy equation. Neglecting the presence of any heat sources, the energy equation can be written as

$$\rho c_p \frac{dT}{dt} = \nabla \cdot (\kappa \nabla T) + T \frac{\partial \boldsymbol{\sigma}}{\partial T} : \nabla \mathbf{v}, \tag{7}$$

where ρ, c_p, κ are the density, specific heat capacity, and the thermal conductivity, respectively. We have assumed, for simplicity, that the specific heat is the same as that for the gas. The first term on the right hand side represents heat diffusion and the second term is work done by stress.

Since we are not considering the gas-phase equations in this work, a constant heat flux is applied from the gaseous phase into the burning solid. A marker function Φ is used to separate the two materials such

that $\Phi = 1$ for AP and $\Phi = -1$ for binder. The heat flux from the gas phase drives the propellant regression, and the corresponding burn rate can be determined as

$$r_b = A \exp\left(-\frac{E_a}{RT_s}\right), \tag{8}$$

where A and E_a are empirical constants, and T_s is the surface temperature. The propellant surface is parameterized by ϕ and is updated by solving the Jacobi–Hamilton equation

$$\phi_t + r_b\sqrt{1+\phi_x^2} = 0. \tag{9}$$

To satisfy conservation of energy across the burning interface, the condition

$$(\kappa\ \mathbf{n}\cdot\nabla T)_g - (\kappa\ \mathbf{n}\cdot\nabla T)_s = -q_s M, \tag{10}$$

must be satisfied, where $()_g$ and $()_s$ refer to the gas and the solid phase quantities, respectively; $M = \rho r_b$ is the mass flux; and q_s is the phase change heat release. Equation (8) together with the jump condition (10) forms a nonlinear system of equations for the surface temperature. Wang *et al.* [6] studied the regression problem for both linear approximation and nonlinear system and did not report any noticeable differences in the solution. In this work, a linear approximation used by utilizing the temperature from previous time step t^n to calculate the burn rate. The heat flux from the gas phase is assumed to be constant; i.e., $(\kappa\mathbf{n}\cdot\nabla T)_g = Q_g$. The jump condition (10) can then be written as

$$\kappa\ \mathbf{n}\cdot\nabla T = Q_g + q_s M, \tag{11}$$

which gives a boundary condition for the surface temperature (T_s). The burn rate can then be computed using equation (8) and is explicitly dependent on surface temperature. The chamber pressure (p_c) is applied as a boundary condition to enforce continuity of momentum at the interface.

2.1. Scaling of Governing Equations

Before proceeding to numerical simulations, it is useful to examine the relevant scales associated with the physical system. Hegab *et al.* [4] presented the length (L) and time (t) scales associated with combustion, where $L = 28 \times 10^{-6}$ m and $t = 2.8 \times 10^{-3}$ s. The characteristic burn rate r_{b0} of the propellant is of the order 1 cm/s. The elastic longitudinal wave speed c_e and shear wave speed c_s are given by

$$c_e = \sqrt{\frac{E}{\rho}}, \qquad c_s = \sqrt{\frac{\mu}{\rho}}, \tag{12}$$

where E is the Young's modulus of the material. Table 1 lists the thermal and mechanical properties of the constituent propellant materials. Given μ and K, E can be calculated as

$$E = \frac{9\mu K}{3K+\mu}. \tag{13}$$

Table 1: Thermal and mechanical properties for propellant constituent materials [12].

Property	**Symbol**	**AP**	**Binder**
Thermal conductivity (W/mK)	κ	0.405	0.276
Activation energy (K)	E_a/R	11000	7500
Heat of reaction (J/kg)	q_s	-47	-100
Arrhenius constant (cm/s)	A	1450	10.36
Bulk Modulus (MPa)	K	14950	10670
Shear Modulus (MPa)	μ	12500	2.5
Density (kg/m^3)	ρ	1950	920
Coeff. of thermal expansion (K^{-1})	α	1×10^{-5}	1×10^{-4}
Wave speed (shear) (m/s)	c_s	2357.4	51.3
Wave speed (longitudinal) (m/s)	c_e	3669.8	88.8

Table 1 lists the elastic wave speeds for constituent materials and these are much larger than the burn rate (r_{b0}). The relevant scales for the problem are chosen as (L, r_{b0}, T_0, E) and the non-dimensional form of the variables can be written as $\tilde{\mathbf{x}} = \mathbf{x}/L$, $\tilde{\mathbf{v}} = \mathbf{v}/r_{b0}$, $\tilde{\boldsymbol{\sigma}} = \boldsymbol{\sigma}/E$, $\tilde{\mathbf{C}} = \mathbf{C}/E$, and $\tilde{t} = tL/r_b$. With these scalings, the hypoelastic equation in non-dimensional form becomes

$$\frac{\partial \tilde{\boldsymbol{\sigma}}}{\partial \tilde{t}} + \tilde{\mathbf{v}} \cdot \tilde{\nabla} \tilde{\boldsymbol{\sigma}} + \tilde{\boldsymbol{\sigma}} \cdot \tilde{\boldsymbol{\omega}} - \tilde{\boldsymbol{\omega}} \cdot \tilde{\boldsymbol{\sigma}} = \tilde{\mathbf{C}} : (\tilde{\mathbf{D}} - \tilde{\alpha} \dot{\tilde{T}}) \tag{14}$$

and the non-dimensional momentum equation is

$$\epsilon \left(\tilde{\rho} \frac{d\tilde{\mathbf{v}}}{d\tilde{t}} \right) = \tilde{\nabla} \cdot \tilde{\boldsymbol{\sigma}} + \tilde{\mathbf{b}}_f, \tag{15}$$

where $\epsilon = \rho_0 r_{b0}^2 / E$ is on the scale of 10^{-4}. This suggests that at the time scales associated with combustion, the mechanical problem is essentially quasi-static. The energy equation in dimensionless form can be written as

$$\tilde{\rho} \frac{d\tilde{T}}{d\tilde{t}} = \frac{1}{Pe} \tilde{\nabla} \cdot (\tilde{\kappa} \tilde{\nabla} \tilde{T}) + \tilde{E} \left(\tilde{T} \frac{\partial \tilde{\boldsymbol{\sigma}}}{\partial \tilde{T}} : \tilde{\nabla} \tilde{\mathbf{v}} \right), \tag{16}$$

where $Pe = \rho_0 c_p L r_{b0} / \kappa_0$ is the Péclet number and $\tilde{E} = E/(\rho_0 c_p T_0)$ is the non-dimensional Young's modulus; both of these parameters are assumed to be $\mathcal{O}(1)$. Using the time scale associated with combustion, the hypoelastic equation (14) and the energy equation (16) remain unchanged, but the momentum equation (15) in the limit $\epsilon \to 0$ becomes

$$\tilde{\nabla} \cdot \tilde{\boldsymbol{\sigma}} + \tilde{\mathbf{b}}_f = \mathbf{0}. \tag{17}$$

In what follows we solve the dimensional forms of (14) for stress, (16) for temperature, and (17) for velocities using a projection method, as will be described in the next section.

2.2. Quasi-static Assumption and Projection Split

Equation (17) is enforced as a constraint on the hypoelastic equation in a manner similar to zero divergence in the incompressible Navier–Stokes equations. These are conducive to the application of the projection method [27] as introduced by Rycroft *et al.* [20]. Consider starting from the stress $\boldsymbol{\sigma}^n$ at timestep t_n, and taking a timestep of size Δt. To perform the projection split, the intermediate stress state $\boldsymbol{\sigma}^*$ is calculated as

$$\frac{\boldsymbol{\sigma}^* - \boldsymbol{\sigma}^n}{\Delta t} = -\mathbf{v}^n \cdot \nabla \boldsymbol{\sigma}^n - \boldsymbol{\sigma}^n \cdot \boldsymbol{\omega}^n + \boldsymbol{\omega}^n \cdot \boldsymbol{\sigma}^n - \mathbf{C} : \mathbf{D}^n_{th}, \tag{18}$$

and the stress update is given by

$$\frac{\boldsymbol{\sigma}^{n+1} - \boldsymbol{\sigma}^*}{\Delta t} = \mathbf{C} : \mathbf{D}^{n+1}. \tag{19}$$

The velocity at t^{n+1} is calculated in the projection step by taking the divergence of equation (19) and enforcing the quasi-static constraint from equation (17). This yields

$$\frac{-\mathbf{b}_f - \nabla \cdot \boldsymbol{\sigma}^*}{\Delta t} = \nabla \cdot (\mathbf{C} : \mathbf{D}^{n+1}). \tag{20}$$

Once the velocity $\mathbf{v}^{n+1}$ is known, the stress $\boldsymbol{\sigma}^{n+1}$ is computed from equation (19).

2.3. Approximate Projection

The projection step (20) yields a coupled Poisson-like equation for the velocity components that contains second-order derivatives. We extend the projection approach to deal with materials having highly disparate material moduli by employing a weak formulation based on the finite-element method. This choice is motivated by the presence of large jump in shear modulus between AP and binder. The framework of solving a weak form of the Poisson equation in otherwise strong form of equations has already been applied to variable density incompressible fluid flows. Almgren *et al.* [28] first introduced a second-order accurate numerical method for incompressible Navier–Stokes equation using an approximate projection with a bilinear basis function for pressure. Instead of forcing the divergence of velocity to be zero in projection step, it is assumed that $\nabla \cdot \mathbf{v} = \mathcal{O}(h^2)$ through the finite-element projection, where h is the grid spacing. The method was extended to variable density flows by Puckett *et al.* [29] with two fluids and large density jumps such as water droplet falling onto a surface. The implementation in this work is based on the application to axisymmetric, incompressible two-phase flows with variable density by Yu *et al.* [30]. Neglecting body forces $\mathbf{b}_f$ in equation (20), the weak form can be obtained by multiplying both sides by a test function w and integrating over the entire domain. This gives

$$-\frac{1}{\Delta t}\int_\Omega w(\nabla \cdot \boldsymbol{\sigma}^*)\, d\mathbf{x} = \int_\Omega w(\nabla \cdot (\mathbf{C} : \mathbf{D}^{n+1}))\, d\mathbf{x}. \tag{21}$$

Applying the divergence theorem to the above equation, we get

$$-\frac{1}{\Delta t}\int_{\delta\Omega} w\boldsymbol{\sigma}^* \cdot \hat{\mathbf{n}}\, dS + \frac{1}{\Delta t}\int_\Omega \nabla w \cdot \boldsymbol{\sigma}^*\, d\mathbf{x} = \int_{\delta\Omega} w(\mathbf{C} : \mathbf{D}^{n+1}) \cdot \hat{\mathbf{n}}\, dS - \int_\Omega \nabla w \cdot (\mathbf{C} : \mathbf{D}^{n+1})\, d\mathbf{x}. \tag{22}$$

To simplify the surface terms, we multiply equation (19) by the test function and integrate over the surface, to obtain

$$-\frac{1}{\Delta t}\int_{\delta\Omega} w\boldsymbol{\sigma}^{*}\cdot\hat{\mathbf{n}}\,dS = -\frac{1}{\Delta t}\int_{\delta\Omega} w\,\boldsymbol{\sigma}^{\mathrm{bc}}\cdot\hat{\mathbf{n}}\,dS + \int_{\delta\Omega} w(\mathbf{C}:\mathbf{D}^{n+1})\cdot\hat{\mathbf{n}}\,dS. \tag{23}$$

Substituting equation (23) into (22), we can write the weak form as

$$\frac{1}{\Delta t}\int_{\delta\Omega} w\,\boldsymbol{\sigma}^{\mathrm{bc}}\cdot\hat{\mathbf{n}}\,dS - \frac{1}{\Delta t}\int_{\Omega}\nabla w\cdot\boldsymbol{\sigma}^{*}\,d\mathbf{x} = \int_{\Omega}\nabla w\cdot(\mathbf{C}:\mathbf{D}^{n+1})\,d\mathbf{x}. \tag{24}$$

The expansion of this equation results in a coupled set of equations for the velocity components, which only have first-order derivatives unlike the strong form (20). The advantage of the weak form over the strong form is that the discretization leads to a symmetric positive definite linear system to solve, where a solution can be guaranteed even for very large density ratios. The details of the numerical discretization and choice of basis function for the approximate projection method are presented in Section 3.

2.4. Reference Map Advection

To calculate strains, an Eulerian framework based on the reference map technique is employed. For any material deforming under load, the motion of a body can be parameterized by a function $\boldsymbol{\chi}$ such that a reference configuration B_o at time $t = 0$ is mapped to the current configuration B at time t. This can be written as

$$\mathbf{x} = \boldsymbol{\chi}(\mathbf{X}, t), \tag{25}$$

where $\boldsymbol{\chi}$ is the motion function mapping points in B_0 to B, $\mathbf{x}$ refers to the current configuration and $\mathbf{X}$ refers to the reference configuration. The deformation gradient associated with the motion function is defined as

$$\mathbf{F} = \nabla\boldsymbol{\chi} = \frac{\partial\mathbf{x}}{\partial\mathbf{X}}. \tag{26}$$

In a Lagrangian description, deformations are explicitly tracked by the motion of material points. In an Eulerian frame, this is done implicitly by specifying an advection equation either directly for the deformation gradient [23, 22] or inverse mapping of the motion function [24]. The reference map technique as introduced by [24] uses an inverse mapping which can be defined as

$$\boldsymbol{X} = \boldsymbol{\chi}^{-1}(\mathbf{x}, t) = \boldsymbol{\xi}(\mathbf{x}, t). \tag{27}$$

Since the reference location for a material point never changes, the constitutive law governing the reference map update can be written as

$$\boldsymbol{\xi}_t + \mathbf{v}\cdot\nabla\boldsymbol{\xi} = \mathbf{0}. \tag{28}$$

The reference map $\boldsymbol{\xi}$ is a continuous mapping from the present configuration of a system to its original/reference position. The deformation gradient using this terminology can be defined as

$$\mathbf{F} = \nabla\boldsymbol{\xi}^{-1}. \tag{29}$$

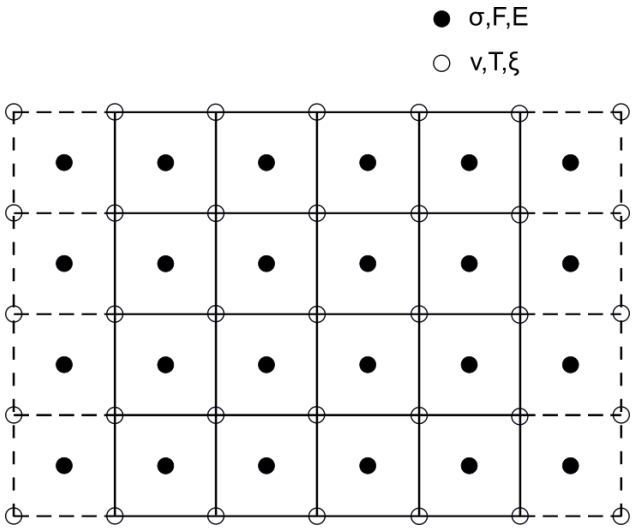

Figure 1: Cartesian grid used for discretization of governing equations.

The Green–St.-Venant strain tensor is related to the deformation gradient by

$$\mathbf{E} = \frac{1}{2}\left(\mathbf{F}^{\mathsf{T}}\mathbf{F} - \mathbf{I}\right). \tag{30}$$

3. Numerical Implementation

In this section, the numerical discretization of the governing equations in two dimensions is presented using finite difference method on a Cartesian grid with n_x and n_y points in the x and y directions, respectively. Figure 1 shows the grid and the staggered discretization of variables used in this work. The velocity $\mathbf{v}$, temperature T, and reference map $\boldsymbol{\xi}$ are located at the grid cell corners, whereas the stress ($\boldsymbol{\sigma}$), the deformation gradient $\mathbf{F}$, and strain tensor $\mathbf{E}$ are located at cell centers. To capture the regressive surface, either of two methods are used. The first method uses a body-fitted grid in physical space that is mapped to a flat surface in the computational domain. This approach works as long as the surface remains single valued, and has been utilized successfully [4, 5]. The advantage of this method is that one-sided difference stencils can be used at the gas–solid surface. Another approach is to describe the surface using a level set that allows for multi-valued surfaces such as found in aluminized propellants [6]. Here, we assume that the surface stays single valued and a mapping is used to map the physical surface to a flat one in the computational domain. The mapped coordinate η can be defined as

$$\eta = y - \phi(x,t), \tag{31}$$

where $\phi(x,t)$ is the surface profile at time t. In addition to capturing the surface profile, it is of interest to capture the thermal boundary layer effects in proximity of the surface. To this end, grid clustering is

employed in the normal direction to the propellant surface by defining another coordinate ($\hat{\eta}$) such that

$$\eta = \frac{\hat{\eta}}{\left(2 - (\hat{\eta}/L_y)^2\right)^{c_{1y}}}, \tag{32}$$

where L_y is the pack length in the y direction and c_{1y} is the clustering coefficient. The coordinate transformation and grid-clustering mapping to capture surface effects keeps the grid is uniform in the computational space $(x, \hat{\eta})$.

3.1. Surface Update

The corrugated surface, parameterized by $\phi(x,t)$ is updated by solving the Jacobi–Hamilton equation (9) using forward Euler time integration

$$\phi^{n+1} = \phi^n - \Delta t\, r_b^n \sqrt{1 + (\phi_x^n)^2}, \tag{33}$$

where the derivative on right hand side is upwinded using a third-oder WENO scheme, and the burn rate r_b is a function of both x and t and is calculated from equation (8).

3.2. Temperature Update

To update temperature, the Crank–Nicolson time stepping scheme is used to numerically integrate the energy equation (7), which can be written as

$$T^{n+1} + \frac{\Delta t}{2} r_1^{n+1} = T^n - \frac{\Delta t}{2} r_1^n + T^n \frac{\partial \boldsymbol{\sigma}}{\partial T}^n : \nabla \mathbf{v}^n, \tag{34}$$

where

$$r_1^s = u^n \frac{\partial T^s}{\partial x} + v^n \frac{\partial T^s}{\partial y} - \frac{1}{\rho c_p}(\nabla \cdot (\kappa \nabla T^s)), \tag{35}$$

for $s = n, n+1$, where the n and $n+1$ superscripts signify the field variables at the respective timestep. It may be noted that a lagged value of velocity components u^n and v^n is used in the convective terms on the left hand side of equation (34). Table 1 lists the thermal properties for the constituent materials and these are located at the cell corners. For example, ρ is treated pointwise; i.e., $\rho_{i,j}$ is used in equation (34). The discretization of equation (34) presented results in a linear system of algebraic equations that is solved using a line relaxation algorithm. More details on numerical discretization can be found in Appendix A.1.

3.3. Stress Update

Assuming two-dimensional plane strain conditions, an elastic material is considered with velocity $\mathbf{v}(\mathbf{x}, t)$ and Cauchy stress tensor $\boldsymbol{\sigma}(\mathbf{x}, t)$, which in component form can be written as

$$\boldsymbol{\sigma} = \begin{bmatrix} \sigma_{11} & \tau & 0 \\ \tau & \sigma_{22} & 0 \\ 0 & 0 & \sigma_{33} \end{bmatrix}, \qquad \boldsymbol{\omega} = \begin{bmatrix} 0 & -\omega & 0 \\ \omega & 0 & 0 \\ 0 & 0 & 0 \end{bmatrix}, \tag{36}$$

where $\omega = \frac{1}{2}(v_x - u_y)$, and x and y subscripts denote partial derivatives with respect to that coordinate direction. Since we have assumed isotropy and constant material coefficients, the right hand side of the hypoelastic relation (1) in component form

$$\mathbf{C} : \mathbf{D} = \begin{bmatrix} (\lambda + 2\mu)u_x + \lambda v_y & \mu(u_y + v_x) & 0 \\ \mu(u_y + v_x) & \lambda u_x + (\lambda + 2\mu)v_y & 0 \\ 0 & 0 & \lambda(u_x + v_y) \end{bmatrix}, \tag{37}$$

and

$$\mathbf{C} : \mathbf{D}_{th} = 3\alpha K \frac{dT}{dt}\mathbf{I}, \tag{38}$$

where $\lambda = K - \frac{2\mu}{3}$. The y derivatives in equation (37) are transformed to $\hat{\eta}$. The first-order forward Euler scheme is used for time integration of the hypoelastic equation (1) and a third-order WENO scheme [31] is used to discretize the advective derivatives on the left hand side for stability. The intermediate stress components $\boldsymbol{\sigma}^*$ at time t^{n+1} are computed as

$$\begin{aligned}
\frac{\sigma_{11}^* - \sigma_{11}^n}{\Delta t} &= -u^n \frac{\partial \sigma_{11}^n}{\partial x} - \bar{v}^n \frac{\partial \sigma_{11}^n}{\partial \hat{\eta}} \frac{d\hat{\eta}}{d\eta} - 2w^n \tau^n - 3\alpha K \frac{dT}{dt}, \\
\frac{\sigma_{22}^* - \sigma_{22}^n}{\Delta t} &= -u^n \frac{\partial \sigma_{22}^n}{\partial x} - \bar{v}^n \frac{\partial \sigma_{22}^n}{\partial \hat{\eta}} \frac{d\hat{\eta}}{d\eta} + 2w^n \tau^n - 3\alpha K \frac{dT}{dt}, \\
\frac{\sigma_{33}^* - \sigma_{33}^n}{\Delta t} &= -u^n \frac{\partial \sigma_{33}^n}{\partial x} - \bar{v}^n \frac{\partial \sigma_{33}^n}{\partial \hat{\eta}} \frac{d\hat{\eta}}{d\eta} - 3\alpha K \frac{dT}{dt}, \\
\frac{\tau^* - \tau^n}{\Delta t} &= -u^n \frac{\partial \tau^n}{\partial x} - \bar{v}^n \frac{\partial \tau^n}{\partial \hat{\eta}} \frac{d\hat{\eta}}{d\eta} + w^n \sigma_{11}^n - w^n \sigma_{22}^n.
\end{aligned} \tag{39}$$

3.3.1. Velocity Update

To compute stress components at t^{n+1}, we need to first compute the velocities. Recall that the weak form of the Poisson equation for velocities can be written as

$$\int_\Omega \nabla w \cdot (\mathbf{C} : \mathbf{D})\, d\mathbf{x} = -\frac{1}{\Delta t} \int_\Omega \nabla w \cdot \boldsymbol{\sigma}^* d\mathbf{x} + \frac{1}{\Delta t} \int_{\delta\Omega} w\, \boldsymbol{\sigma}^{\mathrm{bc}} \cdot \hat{\mathbf{n}}\, dS, \tag{40}$$

where w is an arbitrary test function. To discretize equation (40) on a Cartesian grid, a set of localized basis functions $\psi_{i,j}(\mathbf{x})$ are used. We use piecewise bilinear hat functions $\psi_{i,j}$ is one at (i, j) and zero at all other nodes, and write the velocity as

$$\mathbf{v} = \sum_{i',j'} \mathbf{v}_{i',j'} \psi_{i',j'}(\mathbf{x}), \tag{41}$$

To discretize the right side of equation (40), $\boldsymbol{\sigma}^*$ is assumed to be piecewise constant; i.e., $\boldsymbol{\sigma}^*(\mathbf{x}) = \boldsymbol{\sigma}^*_{i,j}$ on grid cell (i, j). To derive a linear system, we consider each node (i, j) and we put $w = \psi_{i,j}$. Then the integrals in equation (40) will have non-zero contributions for the grid cells S_1, S_2, S_3, and S_4 shown in Figure 2. Thus we can write

$$\sum_{i',j'} \mathbf{v}_{i',j'} \int_\Omega \nabla \psi_{i,j} \cdot (\mathbf{C} : \nabla (\psi_{i',j'}))\, d\mathbf{x} = -\frac{1}{\Delta t} \sum_{i',j'} \left(\int_\Omega \nabla \psi_{i,j} \cdot \boldsymbol{\sigma}^*_{i',j'} d\mathbf{x} + \int_{\delta\Omega} \psi_{i,j} \boldsymbol{\sigma}^{bc}_{i',j'} \cdot \hat{\mathbf{n}}\, dS \right), \tag{42}$$

which leads to a linear system

$$\mathbf{A}\mathbf{v} = \mathbf{B}. \tag{43}$$

where $\mathbf{A}$ is a symmetric positive definite matrix and $\mathbf{v}$ is a vector of all $\mathbf{v}_{i,j}$ components. $\mathbf{B}$ is a source vector arising from the right hand side of equation (42). The two rows in $\mathbf{A}$ corresponding to node (i, j) have non-zero entries for nodes $(i + \alpha, j + \beta)$ where $\alpha, \beta \in \{-1, 0, 1\}$, thus creating a nine-point stencil. We use a Jacobi-preconditioned conjugate gradient method to solve the resulting linear system. The second term

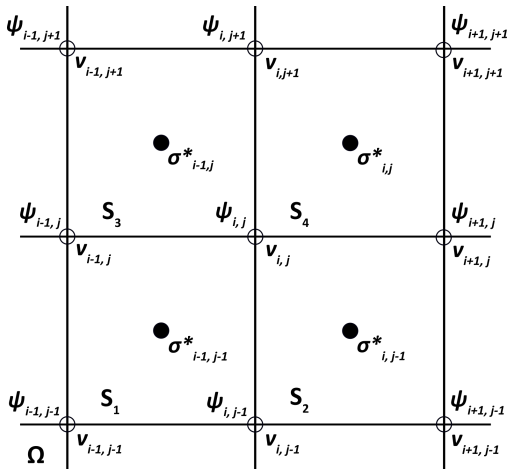

Figure 2: Diagram showing the grid arrangement for calculating the weak form of the projection step on a Cartesian grid. Bilinear hat functions $\psi_{i,j}$ centered on nodes (i, j) are used. When evaluating the weak form for the hat function $\psi_{i,j}$, there will be non-zero contributions from integrating the four grid cells S_1, S_2, S_3, and S_4.

on the right hand side of equation (42) is non-zero only at the domain boundaries since it cancels out on all interior cells. At the top surface, the momentum continuity between the two phases yields the condition $\boldsymbol{\sigma}^{bc} \cdot \hat{\mathbf{n}} = [0 \;\; -p_c \;\; 0]$, where p_c is the chamber pressure on the fluid side. At the bottom surface, we set this term to be zero. The lower boundary has $\mathbf{v} = \mathbf{0}$, while on the top surface the traction boundary condition allows us to solve implicitly for boundary velocities. See Appendix for more details. Once we obtain the velocities, the stress components at time t^{n+1} can be updated according to

$$\begin{aligned}
\frac{\sigma_{11}^{n+1} - \sigma_{11}^*}{\Delta t} &= (\lambda + 2\mu)\left(\frac{\partial u}{\partial x}^{n+1} - \phi_x \frac{d\hat{\eta}}{d\eta}\frac{\partial u}{\partial \hat{\eta}}^{n+1}\right) + \lambda \frac{d\hat{\eta}}{d\eta}\frac{\partial v}{\partial \hat{\eta}}^{n+1}, \\
\frac{\sigma_{22}^{n+1} - \sigma_{22}^*}{\Delta t} &= \lambda\left(\frac{\partial u}{\partial x}^{n+1} - \phi_x \frac{d\hat{\eta}}{d\eta}\frac{\partial u}{\partial \hat{\eta}}^{n+1}\right) + (\lambda + 2\mu)\frac{d\hat{\eta}}{d\eta}\frac{\partial v}{\partial \hat{\eta}}^{n+1}, \\
\frac{\sigma_{33}^{n+1} - \sigma_{33}^*}{\Delta t} &= \lambda\left(\frac{\partial u}{\partial x}^{n+1} + \frac{d\hat{\eta}}{d\eta}\frac{\partial v}{\partial \hat{\eta}}^{n+1} - \phi_x \frac{d\hat{\eta}}{d\eta}\frac{\partial u}{\partial \hat{\eta}}^{n+1}\right), \\
\frac{\tau^{n+1} - \tau^*}{\Delta t} &= \mu\left(\frac{d\hat{\eta}}{d\eta}\frac{\partial u}{\partial \hat{\eta}}^{n+1} + \frac{\partial v}{\partial x}^{n+1} - \phi_x \frac{d\hat{\eta}}{d\eta}\frac{\partial v}{\partial \hat{\eta}}^{n+1}\right).
\end{aligned} \tag{44}$$

3.4. Reference Map

The reference map is initialized on the Cartesian domain of size (n_x, n_y) such that

$$\boldsymbol{\xi} = (\xi_1, \xi_2) = (x, y). \tag{45}$$

The reference map update using a forward Euler integration scheme, and in the computational domain $(x, \hat{\eta})$ can be written as

$$\boldsymbol{\xi}^{n+1} = \boldsymbol{\xi}^n - \Delta t \left(u^n \frac{\partial \boldsymbol{\xi}^n}{\partial x} + \bar{v}^n \frac{d\hat{\eta}}{d\eta} \frac{\partial \boldsymbol{\xi}^n}{\partial \hat{\eta}} \right). \tag{46}$$

The advective derivatives in (46) are upwinded using a second-order ENO scheme. Once the reference map has been updated, the deformation gradient can be computed as

$$\mathbf{F} = \nabla \boldsymbol{\xi}^{-1}. \tag{47}$$

In two dimensions, we can write

$$\mathbf{F} = \frac{1}{\det(\nabla \boldsymbol{\xi})} \begin{bmatrix} \dfrac{d\hat{\eta}}{d\eta} \dfrac{\partial \xi_2}{\partial \hat{\eta}} & -\dfrac{d\hat{\eta}}{d\eta} \dfrac{\partial \xi_1}{\partial \hat{\eta}} \\ -\dfrac{\partial \xi_2}{\partial x} + \phi_x \dfrac{d\hat{\eta}}{d\eta} \dfrac{\partial \xi_2}{\partial \hat{\eta}} & \dfrac{\partial \xi_1}{\partial x} - \phi_x \dfrac{d\hat{\eta}}{d\eta} \dfrac{\partial \xi_1}{\partial \hat{\eta}} \end{bmatrix}, \tag{48}$$

where the gradients are computed using finite differences as

$$\frac{\partial \boldsymbol{\xi}}{\partial x} = \frac{\boldsymbol{\xi}_{i+1,j} - \boldsymbol{\xi}_{i,j}}{\Delta x}, \qquad \frac{\partial \boldsymbol{\xi}}{\partial \hat{\eta}} = \frac{\boldsymbol{\xi}_{i,j+1} - \boldsymbol{\xi}_{i,j}}{\Delta \hat{\eta}}. \tag{49}$$

Once the discretized deformation gradient is computed, equation (30) can be used to calculate strains.

3.5. Time-stepping Summary

To summarize, we generate the grid based on location of surface (ϕ^n) and solve for temperature distribution (34) in the solid using Crank–Nicolson time-stepping scheme. The updated temperature is used to calculate the burn rate (8) and the surface profile (33). The thermal effects are added to the stress equation through an intermediate stress update (39) using forward Euler method and the velocities are computed using a preconditioned conjugate gradient method resulting from weak form discretization of the coupled Poisson-like equation by employing a bilinear basis functions. The stresses at t^{n+1} are updated using equation (44) and the reference map using equation (46) by using a forward Euler update. The strains can be computed using equations (30) and (48).

4. One-Dimensional Verification Studies

In this section, verification results for one-dimensional thermo-mechanical simulations for propellant materials are presented. Each of the constituent material is considered as a one-dimensional homogeneous

strip in the y direction undergoing regression under an applied heat flux and traction on the top boundary. These studies allow for the verification of the numerical solver against analytical solutions. Kuznetsov and Stewart [11] presented thermodynamically consistent hyperelastic formulation for energetic materials, assuming small strains. Under one-dimensional assumptions, the energy equation can be written as

$$\frac{dT}{dy} = \frac{\kappa}{mc_p}\frac{d^2T}{dy^2} - \frac{(\alpha K)^2}{c_p(m^2 - \rho A)}T\frac{dT}{dy}, \tag{50}$$

where $A = \lambda + 2\mu$, $m = \rho r_b$ is the mass flux, and the second term on the right side of equation (50) is the work done by thermal stresses. The burn rate is set to be a constant for this case; i.e., $r_b = 0.45$ cm/s. Equation (50) can be solved numerically given appropriate boundary conditions to obtain the temperature distribution in the homogeneous material. For this study, the lower boundary is maintained at the cold propellant temperature ($T_0 = 300$ K) and a constant heat flux is applied to the top surface ($Q_g = 200$ cal/s $\cdot$ m^2). The top boundary also has an applied traction ($t_s = 2$ MPa), which is equal to the pressure in the gas phase. Once the temperature field is obtained, the deformation gradient F and velocity v are given by [11]

$$F = F_\infty - \frac{\alpha K(T - T_0)}{m^2/\rho_0 - A}, \qquad v = \frac{m}{\rho_0}(F - F_\infty). \tag{51}$$

It is assumed that deep in the propellant, thermal stresses disappear. As a result, the deformation is purely due to applied tractions on the surface. The lower boundary of the propellant is fixed; i.e., $F_\infty = 0$. The stress components are related to temperature and deformation gradient as

$$\sigma_{11} = \sigma_{33} = \lambda F - \alpha K(T - T_0), \tag{52}$$

$$\sigma_{22} = AF - \alpha K(T - T_0), \tag{53}$$

$$p = -\frac{1}{3}(\sigma_{11} + \sigma_{22} + \sigma_{33}), \tag{54}$$

where the pressure p is $-\frac{1}{3}$ of the trace of the stress tensor. Figure 3 shows the comparison between the analytical results of [11] and the present numerical solutions for homogeneous AP. There is excellent agreement between the two. The homogeneous medium develops high pressures due to surface heating (Figure 3b), but the resulting deformation is small (Figure 3d). Figure 4 illustrates the temperature profiles near the surface for homogeneous AP and binder. To maintain similar surface temperature, different heat flux values ($Q_g|_{AP} = 200$ cal/s $\cdot$ m^2, $Q_g|_b = 100$ cal/s $\cdot$ m^2) are chosen. The burn rate is kept constant for both cases ($r_b = 0.45$ cm/s). The contribution of thermal stresses to the temperature distribution is almost negligible for AP (Figure 4a). For binder, the loss in surface temperature due to thermal stresses is much larger (≈ 80 K; Figure 4b). Note that the legend thermal refers to a propellant burning without any thermo-mechanical deformations, which can be obtained by assuming the second term on right hand side of equation (50) to be zero.

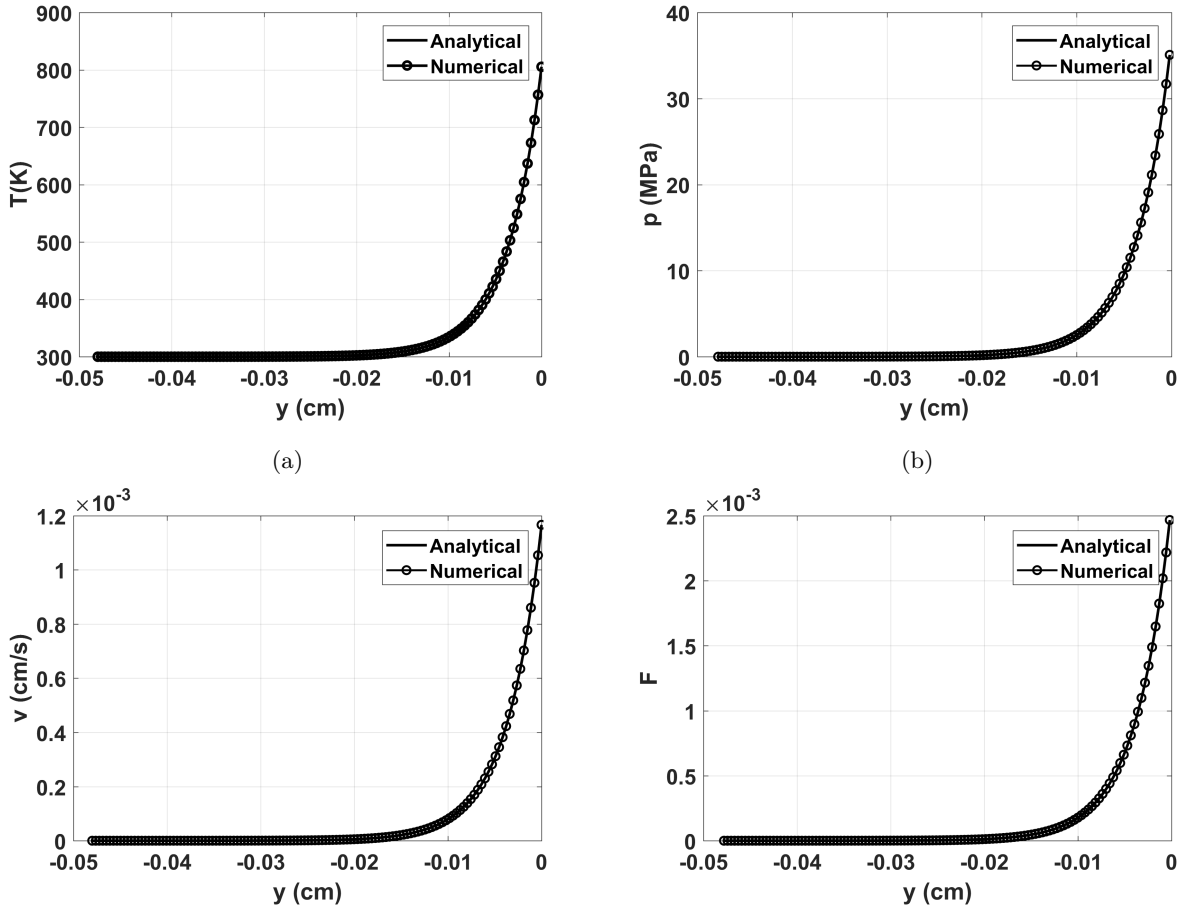

Figure 3: Comparison of (a) temperature, (b) pressure, (c) velocity, and (d) deformation gradient profiles between analytical (solid) and numerical (symbol) solutions for ammonium perchlorate (AP).

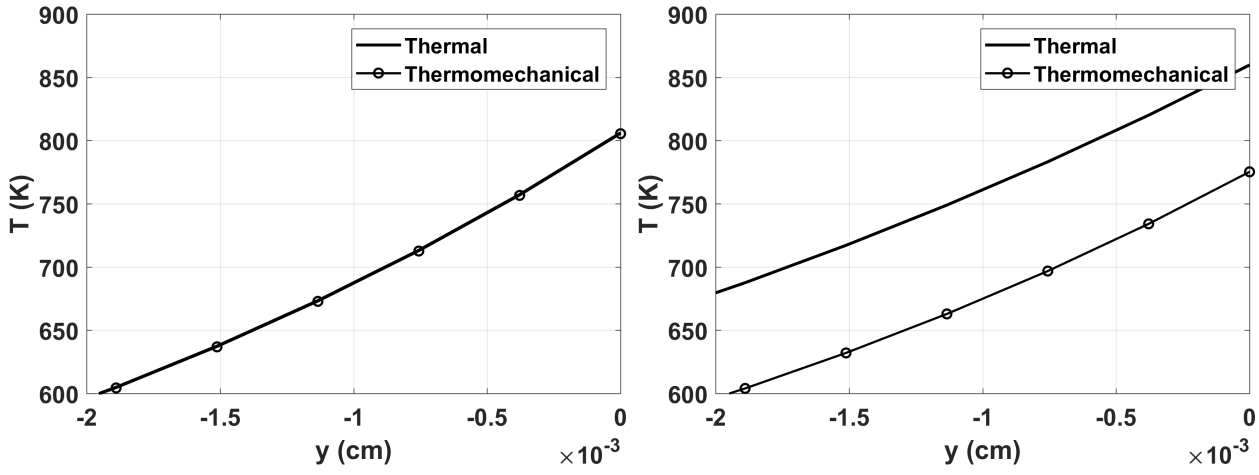

(a) (b)

Figure 4: Temperature profiles in the near-surface region for thermal (solid) and thermo-mechanical (symbol) simulations of homogeneous (a) AP and (b) binder, respectively.

5. Two-Dimensional Results

In this section, results from two dimensional numerical simulations are presented. We first consider a sandwich propellant configuration which consists of a thin piece of binder located between two larger strips of AP. This particular problem has a steady state solution and allows for verification of the numerical solver. Figure 5 illustrates the sandwich problem configuration and the top surface boundary conditions. The pack has length $L_x = 2L$ in the horizontal direction ($-L < x < L$) and $L_y = 4L$ in the vertical direction ($-4L < y < 0$), where $L = 0.012$ cm. The tractions arise from the surface jump condition for momentum continuity between the two phases. In this work, the traction vector is given by $\boldsymbol{\sigma} \cdot \mathbf{n} = (0, -p_c, 0)$, where $p_c = 2$ MPa is the chamber pressure from the gas phase. The pack is assumed to be periodic in the x-direction, and the bottom surface is fixed in y. The center point of the bottom surface is fixed to remove horizontal translations.

Before proceeding to fully coupled thermo-mechanical simulations, we present results for mechanical only simulations of the sandwich propellant subjected to pressure boundary. For this case, there is no heat flux and the surface remains flat. These studies are performed on four different grids of sizes of 32×64, 64×128, 128×256, and 256×512 points. Due to absence of an analytical solution, a high-resolution result on a 512×1024 grid is chosen as the reference solution and interpolated using bilinear interpolation to coarser grids. The error on a particular grid is then computed as the L_2 norm of the difference between the

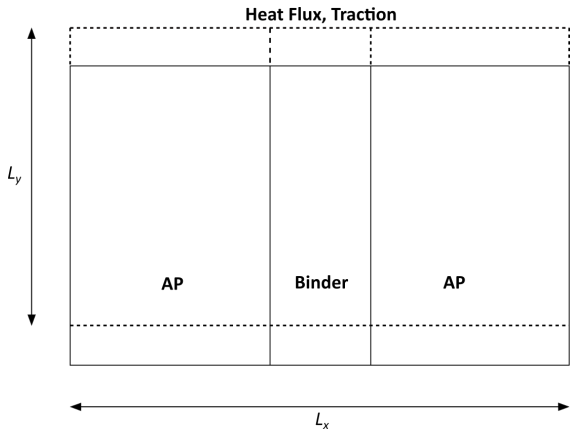

Figure 5: Problem setup for the two dimensional propellant sandwich. The top surface has applied heat flux and traction boundary conditions. The pack is infinitely long in the vertical direction and a window of length L_y is chosen for the numerical simulations. As the pack burns down from the initial (dotted) to the present configuration (solid), the computational grid is regenerated to maintain a fixed window length in the vertical direction.

interpolated solution $f_{i,j}^{\text{interp}}$ and numerical solution $f_{i,j}^{\text{grid}}$, which is given by

$$\epsilon_2 = \sqrt{\frac{\sum_{i,j}(f_{i,j}^{\text{interp}} - f_{i,j}^{\text{grid}})^2}{n_x n_y}}, \tag{55}$$

where $f_{i,j}$ are the values of the field of interest represented on a grid with n_x and n_y points in the horizontal and vertical directions, respectively. Figure 6 shows the convergence of stress and velocity components using the L_2 error norm (55). The dashed and dotted lines represent first and second order convergence, respectively. Using linear curve fitting to discrete error points, the convergence order can be determined as the slope of the line. For stress components $(\sigma_{11}, \sigma_{22}, \sigma_{33}, \tau)$, this order is approximately 1.5. For velocities, this value is 1.90 for u and 1.35 for v.

5.1. Thermo-mechanical simulations

We next present results for coupled thermo-mechanical simulations. The numerical configuration of the test problem is the same as illustrated in Figure 5. A constant heat flux (Q_g) at the top surface drives the propellant regression ($Q_g|_{AP} = 200$ cal/s·m^2, $Q_g|_b = 160$ cal/s·m^2). The pressure from the gas phase $p = 2$ MPa is applied as a traction boundary at the top surface. The temperature at the bottom surface is assumed to be that of a cold propellant $T_{\text{cold}} = 300$ K, and this surface is fixed in the vertical direction ($v = 0$). The reference map is initialized as the Cartesian grid and advected with the velocities. Since the propellant morphology is uniform in y, the problem achieves a steady state solution.

Figure 7 show plots for temperature T, pressure p, and strain $|\mathbf{E}|$ at steady state. Thermal gradients exist in a small layer near the surface, and the pressure and strains are considerably high in this region. It is interesting to note that all of the stress response is restricted to AP, which is compressed due to thermal

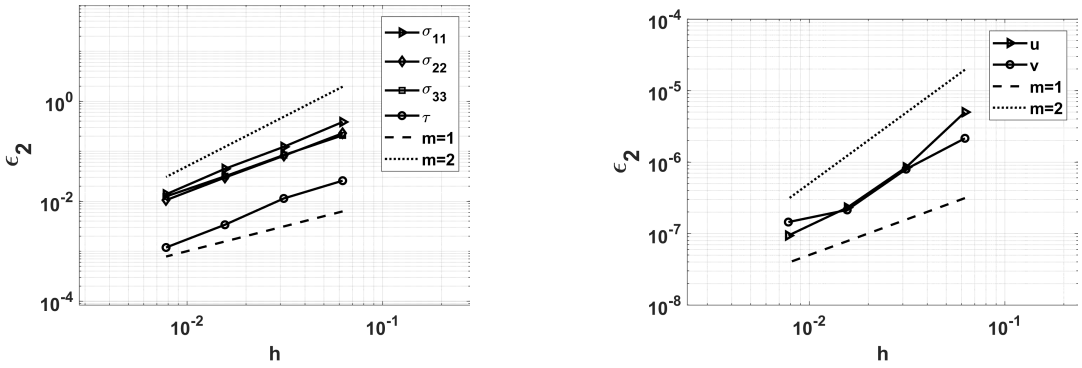

(a) (b)

Figure 6: Plots showing errors computed at different grids for (a) stress and (b) velocity components using the L_2 norm for mechanical simulations. The errors are calculated by considering a 512 × 1024 grid solution as the reference solution. The dashed (m=1) and dotted (m=2) lines represent first and second order convergence, respectively.

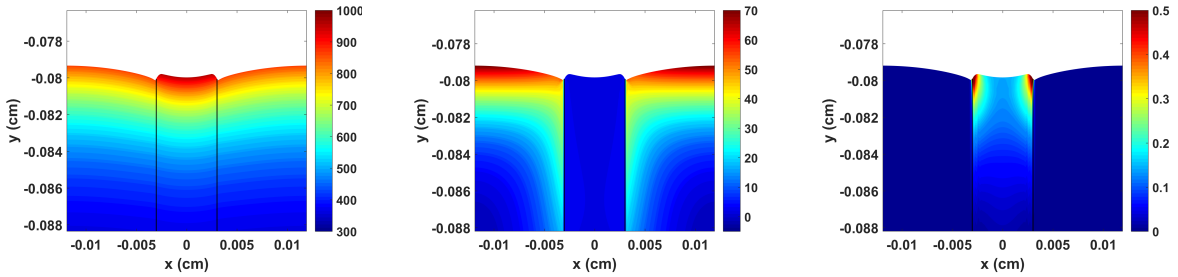

(a) (b) (c)

Figure 7: Plots of (a) temperature (K), (b) pressure (MPa), and (c) strain for the thermo-mechanical sandwich configuration at steady state.

stresses. The interface between two materials experiences strains as high as 50%, and these are highly localized. These strains are of the same order as presented by Srinivasan *et al.* [12]. The presence of large temperature gradients across the AP-binder interface (Figure 8) and moduli mismatch suggests that highly strained regions in the propellant exist at the interfacial boundaries.

To carry out a grid convergence study, we consider a clustered grid with fixed number of grid points in y and vary them in x. This is done primarily to properly resolve the thermal boundary layer. The grid clustering coefficient c_{1y} is fixed at 2, and $n_y = 96$, which gives a minimum grid spacing $\Delta\hat{\eta}_{\min} = 1.25$ µm near the surface. The coarsest grid has 32 points in x and each successive grid has twice the number of the previous grid (64, 128, 256, respectively). The timestep used for numerical integration is $\Delta t = 2 \times 10^{-5}$ s. Figure 8 shows the surface temperature and surface profiles for four different grid sizes. Figure 9 shows the error (ϵ_2) plots for stress, velocity, and reference map components on a log-log plot as a function of grid spacing Δx. The error plots show that a first-order convergence is observed. To compute the error at each

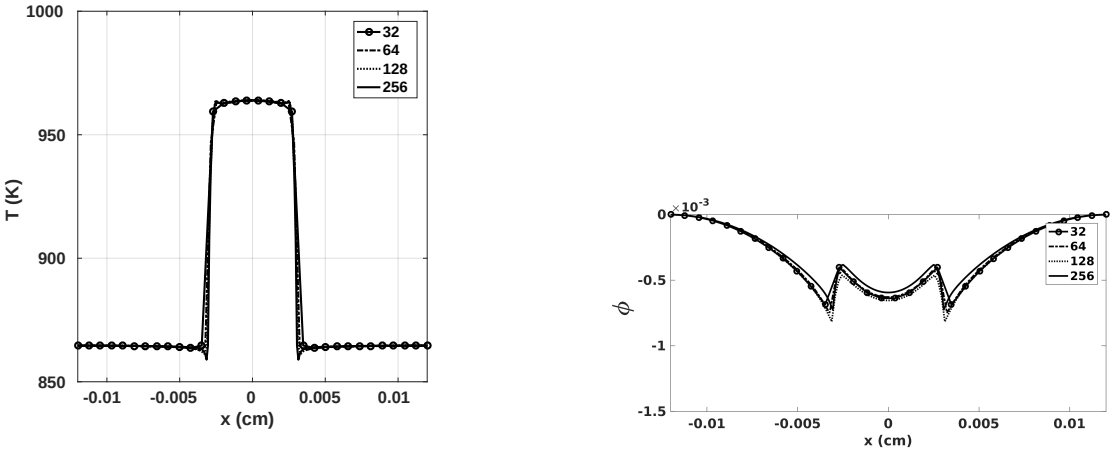

(a) (b)

Figure 8: Plots of (a) surface temperature and (b) surface profile as a function of different grids. The number of points in the y-direction are kept constant for all the grids with a grid stretching factor of $c_{1y} = 2$.

grid, we use the 256×96 grid as the reference solution and interpolate it to each of the coarser grids, and then calculate the error using equation (55).

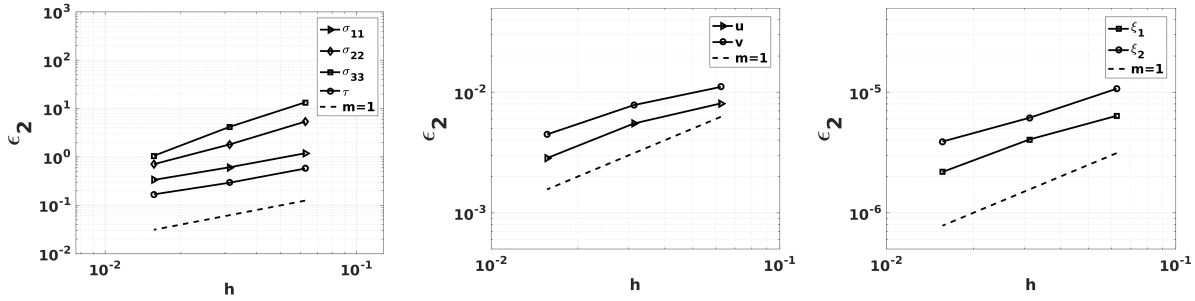

(a) (b) (c)

Figure 9: Plots showing L_2 errors for (a) stress, (b) velocity, and (c) reference map for the thermo-mechanical sandwich problem. The errors are calculated by considering the 256×96 grid solution as reference and interpolating it to coarser grids. The L_2 norm of the error is then computed using the interpolated and actual field data for a particular grid. The dashed line represents first-order convergence.

Figure 10 illustrates thermo-mechanical effects on the temperature and burn rate. For the case when the propellant experiences thermal expansion, a drop in surface temperature is observed (Figure 10a), which causes a drop in the propellant burn rate (plotted as surface averaged burn rate, $\bar{r}_b = \int r_b \, ds / \int ds$; Figure 10b). The temperature drop is much higher in the binder, which is consistent with the observations made for the one dimensional homogeneous cases. However, this drop is not as steep due to heat transfer from neighboring AP strips. The surface experiences outwards expansion, as can be seen in Figure 11, where the

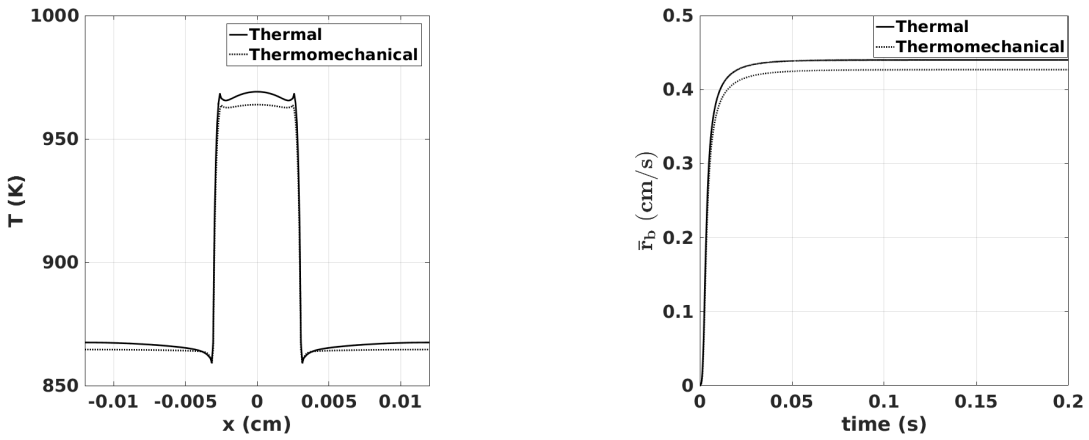

(a) (b)

Figure 10: Plot of (a) surface temperature and (b) surface-averaged burn rate ($\bar{r}_b$) comparison between propellant undergoing thermal (no mechanical effects; solid) and thermo-mechanical regression (thermal expansion and tractions; dash).

steady state surface profile is compared by moving the first grid point to the origin. The maximum outwards displacement is for binder, and is roughly 8 µm.

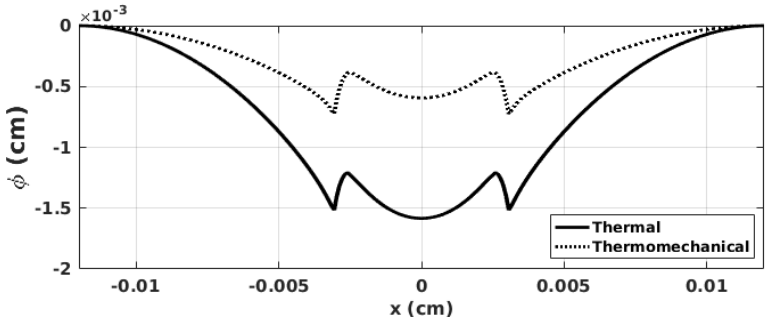

Figure 11: Surface profile at steady state for thermal (solid) and thermo-mechanical (dash) regressing propellants. The first grid point is moved to the origin to make for easier comparison of surface profile and displacement.

5.2. Heterogeneous Random Pack

In this section, results from two-dimensional simulations of random heterogeneous packs are presented. The propellant under investigation consists of AP particles distributed randomly within the binder matrix. This pack is generated using an in-house packing code *Rocpack* [32] with 72% volume fraction of AP particles. Figure 12 illustrates the morphology of the propellant under investigation, which consists of 40 particles of three different diameters (21 of 38.4 µm, 11 of 28.8 µm, 8 of 17.7 µm). The pack is of length $L_x = 2L$ in the x-direction and $L_y = 6L$ in the y-direction, where $L = 0.012$ cm. Simulations are performed on a stretched

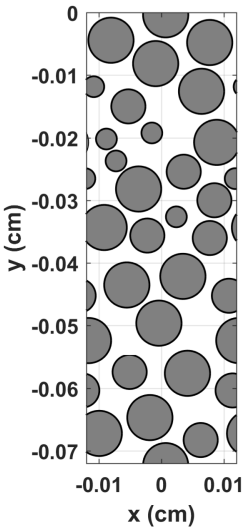

Figure 12: Morphology of the random propellant pack under investigation. The shaded circles represent AP particles randomly distributed in binder matrix (white space). The propellant pack is periodic in the x-direction.

grid (120×96) with $\Delta t = 2.5 \times 10^{-5}$ s and $c_{1y} = 2$. The chosen grid size provides has smallest grid spacing of $\Delta\hat{\eta}_{min} = 2$ µm in the thermal layer. A heat flux is applied on the top surface, such that $Q_g|_{AP} = 200$ cal/s·m^2 and $Q_g|_b = 160$ cal/s·m^2. The surface also experiences loading due to chamber pressure, $p = 2$ MPa. The resulting traction boundary condition determines the top surface velocities implicitly. The pack is periodic in x and semi-infinite in the y-direction. Deep in the propellant, velocities are assumed to be zero and strains to be constant. The reference map is initialized as the coordinates of Cartesian grid and updated using velocities obtained from the Poisson solver. At the bottom, the reference map is fixed in x whereas the y component is advected with the frame speed ϕ_t. The advected map is then used to calculate strains in the propellant pack using equation (30).

Figure 13 shows plots of the temperature, pressure, and strains in the burning propellant at four different times. The strains are restricted within a thin layer near the surface where thermal gradients are large. Furthermore, peak strains occur in thin binder regions in between AP particles, caused by temperature gradient existing between AP-binder interface. This might allude to the effects of randomness and particle size distribution on peak strains.

Figure 15 plots (a) the maximum temperature distribution and (b) the spatially averaged burn rate as a function of time. The dotted line represents the burn rate observed in the pack undergoing thermo-mechanical deformation compared with a pack going purely thermal regression (no deformations). A decrease in burn rate is observed (Figure 15b), which is due to the drop in surface temperatures (Figure 15a) with time averaged value equal to 0.42 cm/s compared with 0.449 cm/s for purely thermal regression. Thermal expansion at the surface causes dissipation of heat, which was also observed in the case of sandwich packs.

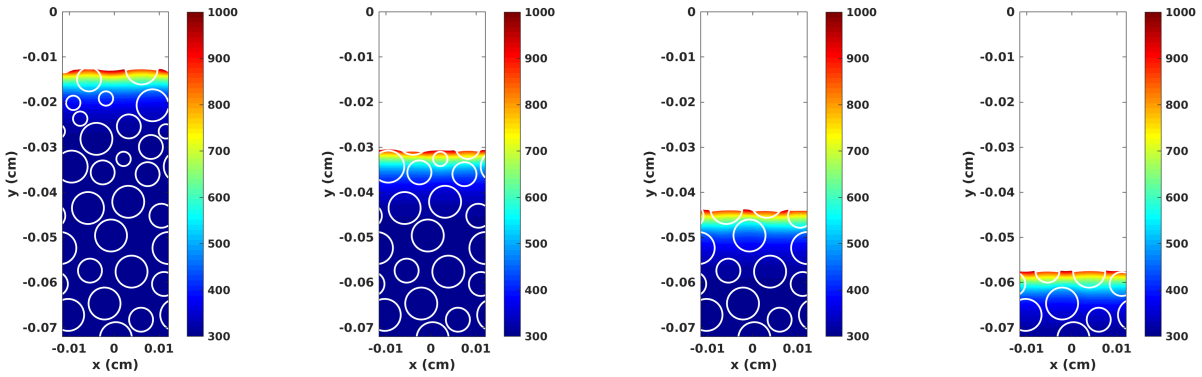

(a) Temperature

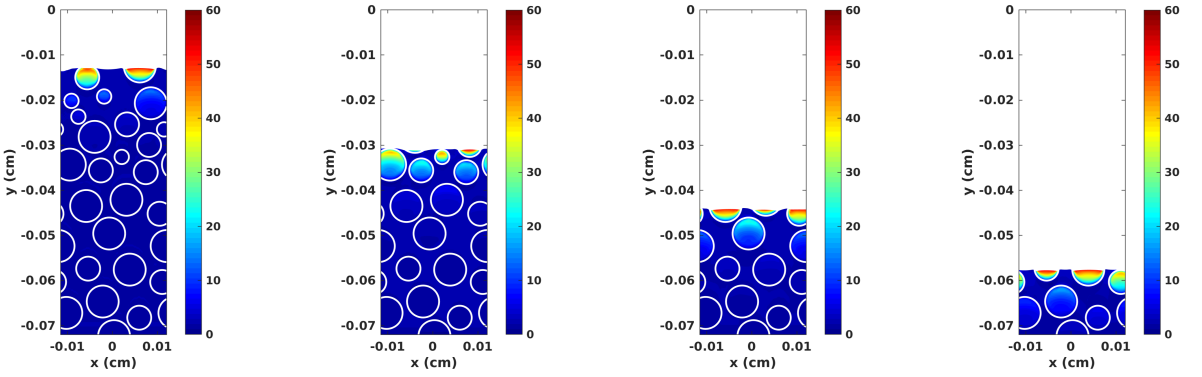

(b) Pressure

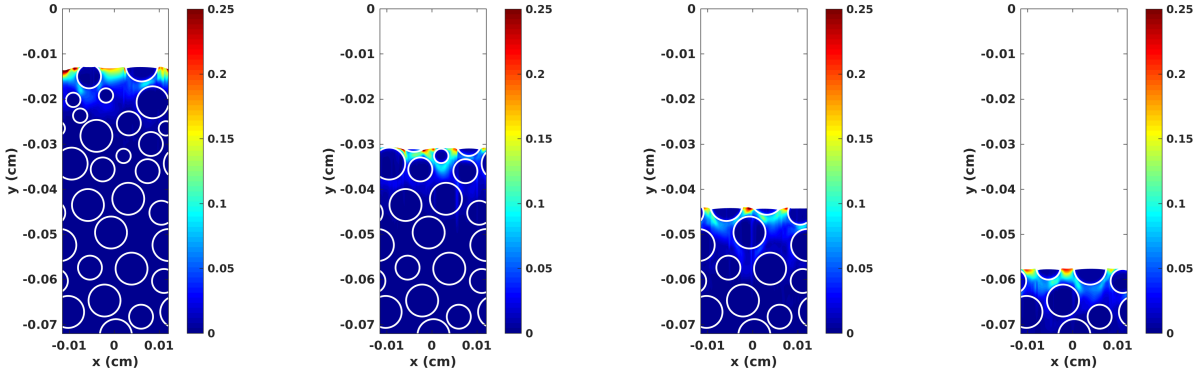

(c) Strains

Figure 13: Plots of (a) temperature (K), (b) pressure (MPa), (c) strains in the random propellant pack undergoing thermal regression at four times ($t = 0.035$ s, 0.075 s, 0.105 s, 0.135 s) from left to right.

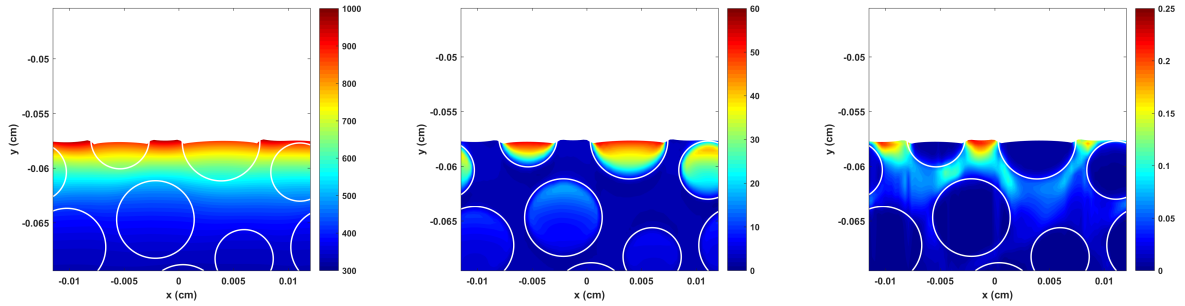

(a) Temperature (b) Pressure (c) Strain

Figure 14: Plots of (a) temperature (K), (b) pressure (MPa), and (c) strain for the random propellant pack undergoing thermal regression at time, $t = 0.135$ s in the vicinity of the propellant surface.

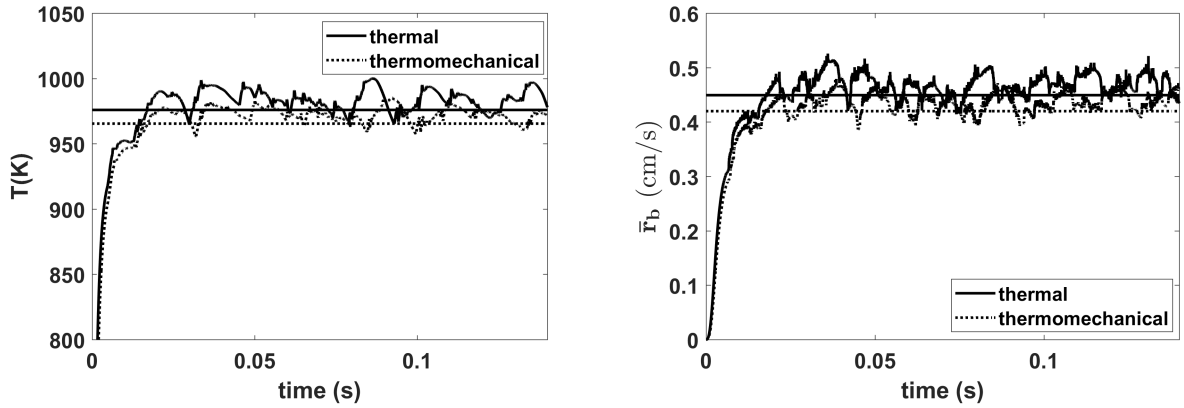

(a) (b)

Figure 15: Plot of (a) the maximum temperature distribution and (b) the surface averaged burn rate as a function of time showing comparison between propellant undergoing thermal (no mechanical effects; solid line) and thermo-mechanical regression (thermal expansion and tractions; dashed line). The straight lines represent the mean values for the time series with $\bar{T} = 975.9$K, $\bar{\bar{r}}_b = 0.449$ cm/s for thermal regression and $\bar{T} = 965.4$K and $\bar{\bar{r}}_b = 0.42$ cm/s for thermo-mechanical regression.

The localized surface swelling brings down the temperature gradient, which results in slower burn rate for the propellant. Finally, the maximum value of the strains is plotted as a function of time in Figure 16. From the figure we see that the averaged peak strain value of 31.6% is smaller than those observed for the sandwich pack ($\approx 50\%$). This drop can be explained by a relatively smooth surface profile for the heterogeneous packs compared with the sandwich.

The random pack simulation is repeated by doubling the applied heat flux values; i.e., $Q_g|_{AP} = 400$ cal/s$\cdot$ m^2 and $Q_g|_b = 320$ cal/s $\cdot$ m^2. Figure 17 shows plots of surface averaged burn rate and maximum strain for this case. The mean burn rate is found to be 0.81cm/s, which is roughly twice of the case with the lower heat flux values. The mean value of the maximum strain is found to be 37.24%, compared with 31.6% for

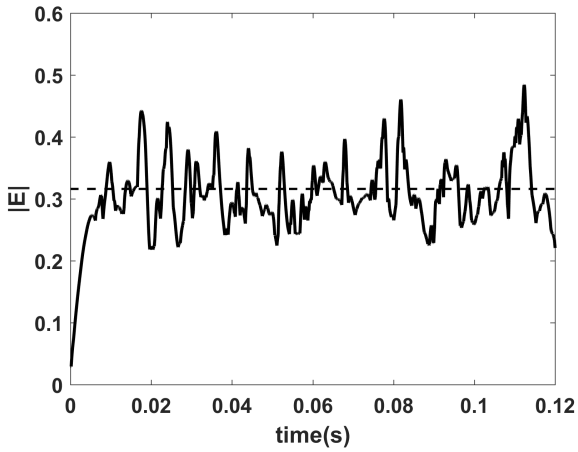

Figure 16: Maximum magnitude of strains plotted as a function of time for the random heterogeneous propellant pack. The dashed line represents the mean value for the time series and is found to be 31.6%.

the lower heat flux values. Due to higher applied heat flux, the strain peaks in Figure 17b are much higher, and in some cases as high as 60%. This suggests an increase in localized strains within the propellant pack as the value of surface heat flux is increased.

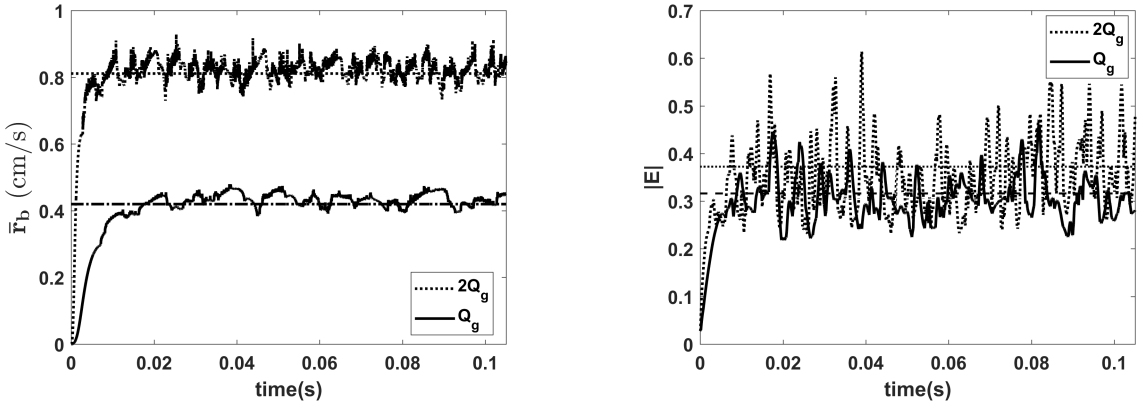

(a) (b)

Figure 17: Plots comparing (a) surface averaged burn rate and (b) maximum strain for two cases of applied heat flux: case 1 (solid, labeled Q_g): $Q_g|_{AP} = 200$ cal/s $\cdot$ m^2 and $Q_g|_b = 160$ cal/s $\cdot$ m^2; case 2 (dash, labeled $2Q_g$): $Q_g|_{AP} = 400$ cal/s $\cdot$ m^2 and $Q_g|_b = 320$ cal/s $\cdot$ m^2. The dashed horizontal lines depict the mean values of the respective time series.

6. Conclusion

In this paper, an Eulerian framework for carrying out thermo-mechanical simulations of heterogeneous propellants based on an approximate projection method is presented. The constituent materials are treated

as hypoelastic solids. Using a scaling argument, a quasi-static form of the governing equations are derived, which involves solving a Poisson equation for the velocities. To address the issue of highly disparate material moduli between AP and binder, the weak form based on finite element projection of the Poisson equation is used. The temperature is obtained from the energy equation and the effect of thermal expansion is accounted for through the stress-work term. The strains are obtained by advecting a reference map.

We first presented one-dimensional verification studies for homogeneous materials and found good agreement between previously published results and our numerical solutions. A grid resolution study for a two-dimensional sandwich configuration was carried out showing convergence rates between first and second orders. Strains as high as 50% at the AP-binder interface were observed. We also compared results between deformation and no deformation cases, and showed that deformation leads to a reduction in both the surface temperature and burn rate. Finally, we carried out two-dimensional simulations of a random heterogeneous propellant pack. Similar to the sandwich configuration, we observed a reduced burn rate when deformation is taken into account. However, the maximum strain is smaller, due to unsteady effects as well as randomness in the locations of the particles.

Since it is well known that the burning rate of a heterogeneous solid propellant is influenced by the propellant morphology, we will carry out three-dimensional thermo-mechanical simulations that can allow for three-dimensional random packs of AP spherical particles. Future work will also account for full coupling between the solid phase and the gas phase, where in the gas-phase the equations for a reactive gas in the low Mach number limit are considered, the thermo-mechanical equations in the solid-phase, and with appropriate jump conditions across the solid/gas interface.

Acknowledgements

T. Kumar and T.L. Jackson were supported in part contract No. FA9300-15-C-0004 issued by the U.S. Air Force Research Laboratory (AFRL) at Edwards Air Force Base, CA, and in part by the U.S. Department of Energy, National Nuclear Security Administration, Advanced Simulation and Computing Program, as a Cooperative Agreement under the Predictive Science Academic Alliance Program, under Contract No. DE-NA0002378. C.H. Rycroft was supported by the National Science Foundation under Grant No. DMS-1753203, and by the Applied Mathematics Program of the U.S. DOE Office of Advanced Scientific Computing Research under contract number DE-AC02-05CH11231. Finally, we would like to acknowledge many fruitful discussions with Mr. Kevin Brown and Dr. Venke Sankaran, AFRL, during the course of this work.

[1] G. P. Sutton, O. Biblarz, Rocket propulsion elements, John Wiley & Sons, 2016.

[2] G. Knott, T. L. Jackson, J. Buckmaster, Random packing of heterogeneous propellants, AIAA Journal 39 (4) (2001) 678–686.

[3] B. D. Lubachevsky, F. H. Stillinger, Geometric properties of random disk packings, Journal of Statistical Physics 60 (5-6) (1990) 561–583.

[4] A. Hegab, T. L. Jackson, J. Buckmaster, D. S. Stewart, Nonsteady burning of periodic sandwich propellants with complete coupling between the solid and gas phases, Combustion and Flame 125 (1-2) (2001) 1055–1070.

[5] L. Massa, T. L. Jackson, M. Short, Numerical solution of three-dimensional heterogeneous solid propellants, Combustion Theory and Modelling 7 (3) (2003) 579–602.

[6] X. Wang, T. L. Jackson, L. Massa, Numerical simulation of heterogeneous propellant combustion by a level set method, Combustion Theory and Modeling 8 (2) (2004) 227–254.

[7] T. L. Jackson, Modeling of heterogeneous propellant combustion: A survey, AIAA Journal 50 (5) (2012) 993–1006.

[8] J. Simo, On a fully three-dimensional finite-strain viscoelastic damage model: Formulation and computational aspects, Computer Methods in Applied Mechanics and Engineering 60 (2) (1987) 153–173.

[9] F. Xu, N. Aravas, P. Sofronis, Constitutive modeling of solid propellant materials with evolving microstructural damage, Journal of the Mechanics and Physics of Solids 56 (5) (2008) 2050–2073.

[10] F. Xu, P. Sofronis, N. Aravas, S. Meyer, Constitutive modeling of porous viscoelastic materials, European Journal of Mechanics-A/Solids 26 (6) (2007) 936–955.

[11] I. R. Kuznetsov, D. S. Stewart, Modeling the thermal expansion boundary layer during the combustion of energetic materials, Combustion and Flame 126 (4) (2001) 1747–1763.

[12] K. R. Srinivasan, K. Matouš, P. H. Geubelle, T. L. Jackson, Thermomechanical modeling of regressing heterogeneous solid propellants, Journal of Computational Physics 228 (21) (2009) 7883–7901.

[13] S. Osher, J. A. Sethian, Fronts propagating with curvature-dependent speed: algorithms based on hamilton-jacobi formulations, Journal of Computational physics 79 (1) (1988) 12–49.

[14] C. H. Rycroft, J. Wilkening, Computation of three-dimensional standing water waves, Journal of Computational Physics 255 (2013) 612–638. doi:10.1016/j.jcp.2013.08.026.

[15] G. Holzapfel, Nonlinear solid mechanics: A continuum approach for engineering science, Chichester, Wiley, New York, 1997.

[16] C. Truesdell, W. Noll, The non-linear field theories of mechanics, in: The non-linear field theories of mechanics, Springer, 2004, pp. 1–579.

[17] L. Tran, H. Udaykumar, A particle-level set-based sharp interface cartesian grid method for impact, penetration, and void collapse, Journal of Computational Physics 193 (2) (2004) 469–510.

[18] A. Kapahi, S. Sambasivan, H. S. Udaykumar, Simulation of collapse and fragmentation phenomena in a sharp interface Eulerian setting, Computers & Fluids 87 (2013) 26–40.

[19] C. H. Rycroft, F. Gibou, Simulations of a stretching bar using a plasticity model from the shear transformation zone theory, Journal of Computational Physics 231 (5) (2012) 2155–2179.

[20] C. H. Rycroft, Y. Sui, E. Bouchbinder, An Eulerian projection method for quasi-static elastoplasticity, Journal of Computational Physics 300 (2015) 136–166.

[21] B. J. Plohr, D. H. Sharp, A conservative Eulerian formulation of the equations for elastic flow, Advances in Applied Mathematics 9 (4) (1988) 481–499.

[22] C. Liu, N. J. Walkington, An Eulerian description of fluids containing visco-elastic particles, Archive for Rational Mechanics and Analysis 159 (3) (2001) 229–252.

[23] P. T. Barton, D. Drikakis, E. I. Romenski, An Eulerian finite-volume scheme for large elastoplastic deformations in solids, International Journal for Numerical Methods in Engineering 81 (4) (2010) 453–484.

[24] K. Kamrin, C. H. Rycroft, J.-C. Nave, Reference map technique for finite-strain elasticity and fluid–solid interaction, Journal of the Mechanics and Physics of Solids 60 (11) (2012) 1952–1969.

[25] L. Adam, J.-P. Ponthot, Thermomechanical modeling of metals at finite strains: First and mixed order finite elements, International Journal of Solids and Structures 42 (21-22) (2005) 5615–5655.

[26] B. A. Boley, J. H. Weiner, Theory of thermal stresses, Courier Corporation, 2012.

[27] A. J. Chorin, Numerical solution of the Navier–Stokes equations, Mathematics of Computation 22 (104) (1968) 745–762.

[28] A. S. Almgren, J. B. Bell, W. G. Szymczak, A numerical method for the incompressible Navier–Stokes equations based on an approximate projection, SIAM Journal on Scientific Computing 17 (2) (1996) 358–369.

[29] E. G. Puckett, A. S. Almgren, J. B. Bell, D. L. Marcus, W. J. Rider, A high-order projection method for tracking fluid interfaces in variable density incompressible flows, Journal of Computational Physics 130 (2) (1997) 269–282.

[30] J.-D. Yu, S. Sakai, J. A. Sethian, A coupled level set projection method applied to ink jet simulation, Interfaces and Free Boundaries 5 (4) (2003) 459–482.

[31] C.-W. Shu, High order ENO and WENO schemes for computational fluid dynamics, in: High-order methods for computational physics, Springer, 1999, pp. 439–582.

[32] G. Amadio, T. L. Jackson, A new packing code for creating mirostructures of propellants and explosives, in: 51st AIAA/SAE/ASEE Joint Propulsion Conference, 2015, p. 4098.